Efficient Insertion of Multiple Objects Parallel Connected by Passive Compliant Mechanisms in Precision Assembly

Dengpeng Xing, Yan Lv, Song Liu, De Xu, and Fangfang Liu

***Abstract*—This paper proposes an efficient strategy to simultaneously insert multiple objects, which are parallel connected by passive compliant mechanisms, in precision assembly. The distinctions of this task include: each object is held compliantly; multiple objects are parallel connected to a manipulator; not all the peg-in-hole has the same insertion condition; and high accuracy is required for each insertion. This configuration can provide sufficient compliance and improve insertion efficiency for massive precision assembly. We model the relationship between the state and force of a single compliant mechanism, and analyze the horizontal compliance of parallel mechanisms. Based on the model, with a fitting and optimization method the states of all but one compliant mechanisms are acquired from microscopic views and the remaining states are optimized with resultant forces provided by a force sensor. To efficiently plan the parallel insertion, we propose a strategy to horizontally compensate according to the resultant force and the horizontal compliance, and to vertically insert based on the insertion ratio expectation, the horizontal offsets of each individual insertion, and the horizontal force. Experiments are carried out to demonstrate the validation of the proposed method.**

***Index Terms*—Efficient insertion, parallel connection, passive compliance, precision assembly.**

I. Introduction

PRECISION assembly handles small-sized objects, achieves high accuracy, and has wide applications in various fields. It differs from traditional assembly in that it grips objects sized millimeters or microns, detects accurate assembly state employing microscopes and micro force sensors, and inserts with precision mechanisms [1]. Precision assembly commonly deals with small-sized, thin-walled, and irregular-shaped objects, which are commonly in interference fit or clearance fit with mere micron-level clearances, and then restriction requirements need to be considered, such as high precision alignment and small range limitation of contact forces.

Precision assembly consists of alignment and insertion and many topics in these aspects are recently investigated. In alignment process, objects are moved to the state where their positions and postures are well aligned [2]. The state detection accuracy is the basis for alignment, and an accurate alignment decreases the burden of insertion. In [3], to increase the attitude detection precision of a slice micropart, a laser triangulation measurement instrument guided by microscopes is used and a calibration method based on nonlinear damping least square method is proposed. To navigate safely in the small operational space, collision detection is also required especially when objects are mutual blocked in vision. In [4], an efficient strategy is proposed to obtain the cylindrical object's collision status based on two planar views provided by microscopes, and a detach controller is designed in case of collision. After insertion starts, the contact part is covered and no longer available to visual methods, and as a result force based approaches are used to compensate for the misalignment [5]. In this process, how to define a controller in facilitating precise, robust, and efficient insertions is focused. To increase assembly robustness, inclined insertion is studied in [6] where deviated insertion estimation and coordinated compensation are processed. For efficiency improvement, a stochastic model is built to describe the uncertainty in insertion and a planning method is proposed to choose an efficient action based on estimation results [7]. In precision assembly tasks, most objects are rigidly gripped, and adding compliance in insertion as well as improving efficiency for massive assembly still need to be further explored.

Compliance in insertion helps to protect objects and it is classified into active compliance and passive compliance. Active compliant strategies usually use rigid clamping, such as absorbing with vacuum mechanisms [8] or piezoelectric actuator [9], to hold objects and actively compensate for misalignment based on contact force. Passive compliance, on the contrary, is realized via mechanisms and objects are automatically adjusted according to the contact on the passive degree of freedoms (DOFs)

Manuscript received March 15, 2018; revised October 26, 2018 and January 7, 2019; accepted January 26, 2019. Date of publication February 5, 2019; date of current version September 3, 2019. This work was supported in part by the Science Challenge Project under Grant TZ2018006-0204-02 and in part by the National Nature Science Foundation of China under Grant 61673382, Grant 61873266, and Grant 61733004. Paper no. TII-18-0673. *(Corresponding author: Fangfang Liu.)*

D. Xing, D. Xu, and F. Liu are with the Institute of Automation, Chinese Academy of Sciences, Beijing 100195, China (e-mail: dengpeng.xing@ia.ac.cn; de.xu@ia.ac.cn; fangfang.liu@ia.ac.cn).

Y. Lv is with the School of Engineering, Zhejiang A&F University, Hangzhou 311300, China (e-mail: lvyan@zju.edu.cn).

S. Liu is with the Department of Electrical Engineering-Electrophysics, University of Southern California, Los Angeles, CA 90089, USA (e-mail: liusong@usc.edu).

Color versions of one or more of the figures in this paper are available online at http://ieeexplore.ieee.org.

Digital Object Identifier 10.1109/TII.2019.2897731

[10]. This type of insertion allows relatively large alignment errors and provides an opportunity for quick and stable insertions. The compliant gripper varies according to different objects and tasks, and has the difficulty of generalized application. Low translational and rotational stiffness is offered in [11] by a micro gripper with a micro remote center compliance unit, so that no microscopy is used. A compliant gripper that possesses a large gripping range with a bidirectional drive is presented in [12] to accommodate the grasp of different object size and weight. In [13], a two ionic polymer metal composite fingers based micro gripper is used to add compliance into the assembly robot arm and the errors computed based on the analytical model are compensated. These passive compliant mechanisms are designed to grip one object at a time, which results in low efficiency, and unsuitable for massive assembly tasks.

Serial assembly is common, procedurally performing object gripping, aligning, inserting, and releasing, and it executes one assembly after another. For example, in [14], five subassemblies are sequently realized on one assembly platform and the micromanipulation space only accommodates one pair of objects. Parallel assembly simultaneously handles two or more object alignments and insertions, and its motion planning needs to consider all peg-in-hole as a whole, not just one pair. This assembly type has high efficiency compared with serial counterpart and is suitable for massive assembly [15], [16], but it has more requirements on the control strategy. In [17], a parallel microassembly approach is proposed to grasp and assemble three windings simultaneously for increasing productivity. Chang *et al.* [18] introduces a massive parallel assembly of microchips with water mist, and a hybrid approach is used for high accuracy and speed achievement. An approach is introduced in [19] to parallel assemble on a silicon micro electro mechanical system to lower assembly costs while maintaining high precision. In these parallel assembly works, objects are rigidly gripped and the insertion stiffness is very large, demanding high requirements on initial setting, objects manufacturing, and system accuracy. How to improve insertion compliance is one focus of parallel assembly.

As stated above, compliant mechanisms can improve insertion compliance with low efficiency while parallel configurations fasten the assembly of massive objects with large insertion stiffness and high initialization requirements. Therefore, this paper combines these two together in precision assembly and intends to deal with a parallel insertion of multiple objects connected by passive compliant mechanisms. We choose spring as the compliant mechanism due to its flexibility of compression, transverse, and bending, analyze the compliance of parallel springs, and build a model to relate the spring state with its force. Spring states are used to reflect the contact status for each insertion, and to acquire them we use microscopes to observe all but one springs whose offsets are computed with a fitting and optimization method and a force sensor to obtain the resultant force with which to optimize the rest spring's state. In simultaneous insertion of multiple objects, the horizontal compensation is based on the resultant force and the horizontal stiffness, and the vertical insertion is efficiently planned based on the insertion ratio expectation, the spring horizontal offset, and the horizontal force. The proposed method is verified in experiments.

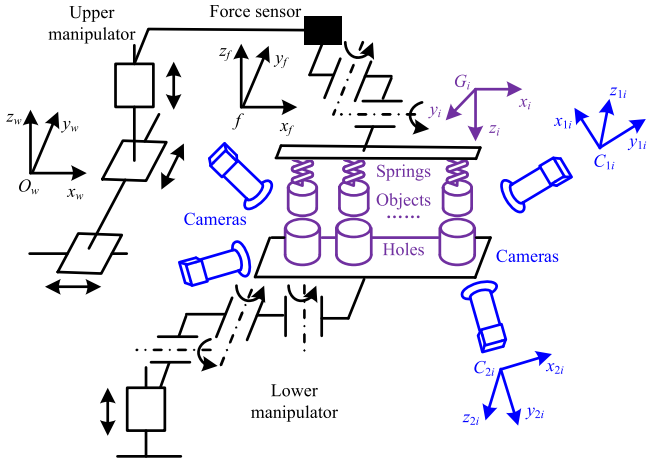

Fig. 1. Platform configuration.

The main contributions include: first, in precision assembly, we investigate on parallel insertion of multiple objects connected by passive compliant mechanisms. This new configuration can provide sufficient compliance and improve insertion efficiency for massive assembly. Second, a fitting and optimization method based on the built spring model is proposed to detect spring state when its ends are not available in images. Third, an efficient strategy for parallel compliant insertion is presented to adjust the insertion depth increment based on the previous insertion performance, the current offset error, and the resultant contact.

There are many situations to apply the method presented in this paper. In order to improve assembly efficiency in engineering, multiple insertions, instead of a single peg-in-hole, are handled in the meantime and the assembly stiffness increases with the object number in one batch. Since objects are brittle in precision assembly, the passive compliance is required for protection, but how to distinguish each insertion state is still difficult. The proposed method addresses these difficulties by obtaining states with graphical and optimization approaches and plans the parallel passive insertion efficiently.

II. System Configuration

A basic platform configuration for parallel compliant assembly is shown in Fig. 1, which consists of upper and lower manipulators, cameras, a force sensor, and upper and lower grippers. The upper manipulator has three translational DOFs and two rotational DOFs to fulfill alignment and insertion; the lower manipulator has one translational DOF and three rotational DOFs for posture alignment; a force sensor locates upon the upper gripper to detect the resultant force that holes execute upon objects; each of n objects is connected via a spring to the upper manipulator; n holes are held still on the lower manipulator; and all microscopes are placed horizontally.

For convenience, we name group i as the combination of the spring i, the object i, and the hole i. All objects are cylinder shaped and they may not have the same diameters, but their lengths are identical. The springs have the same free length and

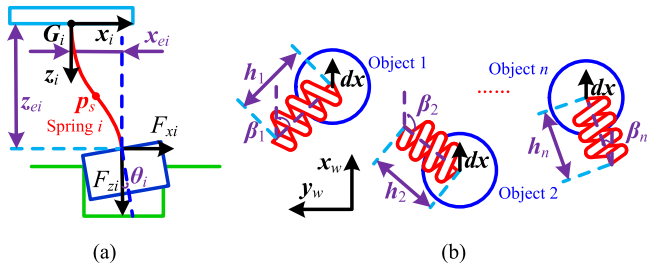

Fig. 2. Spring configuration in insertion. (a) Single insertion. (b) Insertions viewed from the top.

their ends are perpendicularly fixed on the upper manipulator and the object in the same group. The holes have the same sizes with their corresponding objects. All these theoretically provide the same condition for each group insertion, but in practice they are inevitably not the same, e.g., the offsets of springs' ends may differ caused by initialization errors. The microscope has characteristics of planar vision, and during insertion we use $2(n-1)$ microscopes to observe $n-1$ springs. The target is to simultaneously insert n objects into n holes.

The world coordinates $\{W\}$ are established on the upper manipulator; for group i a coordinate frame $\{G_i\}$ is set at the i spring's top end with x_i-axis horizontally pointing to the bottom end and z_i-axis downwards; $\{C_{1i}\}$ and $\{C_{2i}\}$ represent the coordinates on the two horizontal microscopes observing the spring i; and the coordinates $\{f\}$ are established on the force sensor.

III. Compliance Discussion

A. State Computation of a Single Spring

During insertion, the spring is in compression, and in the first several insertion steps when the hole has not limited the object's posture, the object may be a little inclined if the spring is deviated, as shown in Fig. 2(a). We use a general model to bridge the spring state and force. In insertion, the spring is perpendicular to the upper manipulator and the object; the upper manipulator does not rotate; and the object's posture can only deviate very little. As a result, the spring bends if there exists a horizontal offset between spring's ends. Suppose the spring is homogeneous, which leads to the same bending degree of every part of the spring, and use a cubic function to approximate the spring curve based on the distance between its two ends.

In the plane of $G_i - \boldsymbol{x}_i\boldsymbol{z}_i$, as shown in Fig. 2(a), label $p_{ei} = [x_{ei}, z_{ei}]^{\mathrm{T}}$ as the position of the spring's bottom end and $[F_{xi}, F_{zi}]^{\mathrm{T}}$ as the spring force. The spring curve is

$$x_i = a_i z_i^3 + b_i z_i^2 + c_i z_i + d_i \tag{1}$$

where a_i, b_i, c_i, and d_i are function parameters, and $[x_i, z_i]^{\mathrm{T}}$ is the position of a point on the spring curve. Label θ_i as the angle between the object's axis and the $\boldsymbol{z}_i$-axis. According to the position and slop of the spring's two ends, the function parameters result in

$$a_i = \frac{\tan\theta z_{ei} - 2x_{ei}}{z_{ei}^3}, \quad b_i = \frac{3x_{ei} - \tan\theta z_{ei}}{z_{ei}^2}, \quad c_i = d_i = 0. \tag{2}$$

See Appendix A for solution details. The spring length yields

$$L_i = \int_0^{z_{ei}} \sqrt{1 + \left(3a_i z_i^2 + 2b_i z_i\right)^2} dz_i \tag{3}$$

where L_i is the spring length. The homogeneous property leads to the same stiffness for every part of the spring and the vertical force is acquired by integrating the force projection of every part of the spring onto the $\boldsymbol{z}_i$-axis

$$F_{zi} = \int_0^{L_i} K\frac{L_0 - L_i}{L_i}\cos\alpha_l dl_i = K\left(\frac{L_0}{L_i} - 1\right) z_{ei} \tag{4}$$

where K is the spring stiffness, L_0 is the spring length with no load, and α_l is the angle between the spring at l_i and the $\boldsymbol{z}_i$-axis. In the same way, the horizontal force can be obtained

$$F_{xi} = K\left(\frac{L_0}{L_i} - 1\right) x_{ei}. \tag{5}$$

B. Compliance Analysis of Parallel Springs

In insertion, the springs may not deviate in the same direction and we need first to analyze the three dimensional compliance of a spring. Project the springs onto the horizontal plane, as shown in Fig. 2(b), and label β_i as the angle between the projection of the spring i and the $\boldsymbol{x}_w$-axis. As to the spring i, its compression contributes to the force in the $\boldsymbol{x}_w$-axis

$$F_{i,x} = K\left(\frac{L_0}{L_i} - 1\right) h_i \cos\beta_i \tag{6}$$

where $F_{i,x}$ is the force projection of the spring i onto the $\boldsymbol{x}_w$-axis and h_i is the spring's projection length on the horizontal plane. With a virtual displacement dx_w, this force changes to

$$F'_{i,x} = K\left(\frac{L_0}{L'_i} - 1\right)\left(h_i\cos\beta_i + dx_w\right) \tag{7}$$

where $F'_{i,x}$ is the virtual force of the spring i and L'_i is the spring's length corresponding to the virtual displacement. Usually, the vertical offset of the spring far outweighs its horizontal offset since in precision assembly the misalignment is counted by microns, and therefore we use L_i to replace L'_i. Combining the above two equations leads to

$$K_{hi,x} = \frac{dF_{i,x}}{dx_w} = \frac{F'_{i,x} - F_{i,x}}{dx_w} = K\left(\frac{L_0}{L_i} - 1\right) \tag{8}$$

where $K_{hi,x}$ is the horizontal stiffness in the $\boldsymbol{x}_w$-axis. Since this stiffness does not depend on the angle β_i, it means the spring stiffness is the same in the horizontal plane

$$K_{hi} = K\left(\frac{L_0}{L_i} - 1\right) \tag{9}$$

where K_{hi} is the horizontal stiffness of the spring i.

The horizontal stiffness of a parallel configuration is the sum of all the springs' stiffness

$$K_h = \sum_{i=1}^{n} K_{hi} \tag{10}$$

where K_h is the horizontal stiffness of n parallel springs.

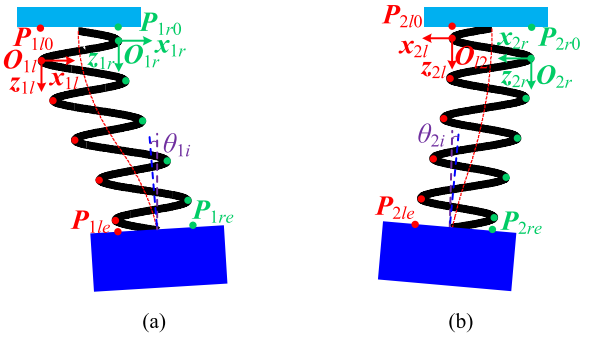

Fig. 3. Views of the group i in two microscopes. (a) Viewed in the camera c_{1i}. (b) Viewed in the camera c_{2i}.

IV. Spring State and Force Acquisition

Two microscopes are needed to observe a spring, due to the characteristics of the planar vision. To reduce costs, we use $2\,(n-1)$ microscopes to detect $n-1$ springs' states and a force sensor to output the resultant force exerted on all objects. With captured images, this paper presents a graphical measurement to detect the spring state fitting the key points on a spring with the above proposed model; and after acquiring the $n-1$ springs' states, an optimization approach is discussed to compute the last spring's state based on the resultant force. This section aims at obtaining the states of every insertion group, which will be an element to be considered in insertion planning.

A. Vision-Based State Acquisition

The object is in stationary balance for every insertion step, and although its contact with the hole is unobservable we still can acquire it using the above established model based on the spring observation. Fig. 3 shows the two views of the group i in the microscopes, c_{1i} and c_{2i}. In Fig. 3, the object's slopes are labeled as θ_{1i} and θ_{2i}, which can be obtained by fitting the object's outline.

The two ends of the spring are usually welded or glued to firmly connect to the manipulator and the object, and as a result the end points cannot be directly detected (which can be seen in experiment). We use multiple points to fit the spring's curve and then determine the offset between the end points. Label the left points of the spring in the image of the camera c_{1i} as $P_{1lj}=[x_{1lj},z_{1lj}]^{\mathrm{T}}$, as the red points shown in Fig. 3(a), where $j\in[1,m_{1l}]$ with m_{1l} as the number of left points in this image. To get those left points, in image processing, we use Canny operator to locate the edge points and circular Hough Transform to obtain the circle parameters. The coordinates $\{O_{1l}\}$ are set as: the origin at the upmost point P_{1l1}, the $\boldsymbol{x}_{1l}$-axis pointing to the right, and the $\boldsymbol{z}_{1l}$-axis pointing downwards. Based on the assumption that the spring's axis can be expressed as piecewise quadratic functions, the axis projection onto the view plane can also be fitted in the same way. It can also be applied to the left points of the spring, which yields

$$^{c}x_{1lj}-x_{1l0}=a_{1l}\left(z_{1lj}-z_{1l0}\right)^{3}+b_{1l}\left(z_{1lj}-z_{1l0}\right)^{2} \tag{11}$$

where $^{c}x_{1lj}$ means the computed value on the $\boldsymbol{x}_{1l}$-axis when fitting the left points and $P_{1l0}=[x_{1l0},z_{1l0}]^{\mathrm{T}}$ is the point, above the coordinate origin, on the fitting curve whose slope is zero. Label $P_{1le}=[x_{1le},z_{1le}]^{\mathrm{T}}$ as the point on the fitting curve with the slope of $\tan\theta_{1i}$, and substituting $P_{1le}-P_{1l0}$ to replace x_{ei} and z_{ei} in (2) results in the function parameters a_{1l} and b_{1l}. The unknown variables are computed by optimizing the error between the fitting data and the true values

$$\min_{P_{1l0},P_{1le}}\sum_{j=1}^{m_{1l}}\|^{c}x_{1lj}-x_{1lj}\|. \tag{12}$$

SNOPT is a general purpose system for constrained optimization, using sequential quadratic programming, and we apply it in acquiring optimized values in this paper.

In the same way, we can compute the two end positions of the fitting curve of the right points, $P_{1r0}=[x_{1r0},z_{1r0}]^{\mathrm{T}}$ and $P_{1re}=[x_{1re},z_{1re}]^{\mathrm{T}}$. Averaging the offsets of the two fitting curves yields

$$\Delta x_{1i}=\frac{(x_{1le}-x_{1l0})+(x_{1re}-x_{1r0})}{2},\Delta z_{1i}=\frac{(z_{1le}-z_{1l0})+(z_{1re}-z_{1r0})}{2} \tag{13}$$

where Δx_{1i} and Δz_{1i} are the offsets of the spring's center in the view of the camera c_{1i}. By iterating the above process, the offsets viewed in the other camera, Δx_{2i} and Δz_{2i}, are obtained. Label $^{1i}\boldsymbol{R}_{w}=[^{1i}\boldsymbol{R}_{w,1}^{\mathrm{T}},{}^{1i}\boldsymbol{R}_{w,2}^{\mathrm{T}},{}^{1i}\boldsymbol{R}_{w,3}^{\mathrm{T}}]^{\mathrm{T}}$ to represent the transformation matrix from the world coordinates to the coordinates of the camera c_{1i}, and $^{2i}\boldsymbol{R}_{w}=[^{2i}\boldsymbol{R}_{w,1}^{\mathrm{T}},{}^{2i}\boldsymbol{R}_{w,2}^{\mathrm{T}},{}^{2i}\boldsymbol{R}_{w,3}^{\mathrm{T}}]^{\mathrm{T}}$ transforming from the world coordinates to $\{C_{2i}\}$. The spring offset in the world coordinates results in

$$\begin{bmatrix}{}^{w}x_{ei}\\{}^{w}y_{ei}\\{}^{w}z_{ei}\end{bmatrix}=\begin{bmatrix}{}^{1i}\boldsymbol{R}_{w,1}\\{}^{1i}\boldsymbol{R}_{w,3}\\{}^{2i}\boldsymbol{R}_{w,1}\\{}^{2i}\boldsymbol{R}_{w,3}\end{bmatrix}^{\dagger}\begin{bmatrix}\Delta x_{1i}\\\Delta z_{1i}\\\Delta x_{2i}\\\Delta z_{2i}\end{bmatrix} \tag{14}$$

where $[{}^{w}x_{ei},{}^{w}y_{ei},{}^{w}z_{ei}]^{\mathrm{T}}$ is the vector pointing from the spring's top end to its bottom end, expressed in the world coordinates, and $\dagger$ is the pseudoinverse. Since the setup of $\{G_i\}$ is based on the spring offset, the transformation matrix $^{G_i}\boldsymbol{R}_{w}$ from the world coordinates to $\{G_i\}$ yields

$$^{G_i}\boldsymbol{R}_{w}=\begin{bmatrix}\frac{{}^{w}x_{ei}}{\sqrt{{}^{w}x_{ei}^{2}+{}^{w}y_{ei}^{2}}} & \frac{{}^{w}y_{ei}}{\sqrt{{}^{w}x_{ei}^{2}+{}^{w}y_{ei}^{2}}} & 0\\ -\frac{{}^{w}y_{ei}}{\sqrt{{}^{w}x_{ei}^{2}+{}^{w}y_{ei}^{2}}} & \frac{{}^{w}x_{ei}}{\sqrt{{}^{w}x_{ei}^{2}+{}^{w}y_{ei}^{2}}} & 0\\ 0 & 0 & 1\end{bmatrix}. \tag{15}$$

The offsets of the spring i result in $x_{ei}=\sqrt{{}^{w}x_{ei}^{2}+{}^{w}y_{ei}^{2}}$ and $z_{ei}={}^{w}z_{ei}$, with which the spring stiffness is computed resorting to the previous section.

In the coordinates $\{C_{1i}\}$, the vector that is perpendicular to the object's axis projection and lies in the view plane can be expressed as $[-\cos\theta_{1i},0,\sin\theta_{1i}]^{\mathrm{T}}$. With the object's slopes in the two images, its posture vector yields

$$\begin{aligned}{}^{w}\boldsymbol{d}=&\,{}^{1i}\boldsymbol{R}_{w}^{-1}\left[-\cos\theta_{1i},0,\sin\theta_{1i}\right]^{\mathrm{T}}\\&\times{}^{2i}\boldsymbol{R}_{w}^{-1}\left[-\cos\theta_{2i},0,\sin\theta_{2i}\right]^{\mathrm{T}}\end{aligned} \tag{16}$$

where ${}^{w}\boldsymbol{d}$ is the vector parallel with the object's axis, expressed in the world coordinates, and "$\times$" is the cross product. The angle between the spring and the vertical axis leads to

$$\theta_i = \arccos\left(\frac{{}^{w}\boldsymbol{d}}{\|{}^{w}\boldsymbol{d}\|_2}\cdot\boldsymbol{z}_w\right) \tag{17}$$

where "$\cdot$" is the dot product. With the solved spring offset, resorting to (4) and (5), the current forces on the spring i, $F_{xi,k}$, and $F_{zi,k}$, are computed, where "k" stands for the discrete insertion step. Expressing them in vectors of the world coordinates results in

$$\boldsymbol{F}_{vi,k} = F_{zi,k}\boldsymbol{z}_w, \quad \boldsymbol{F}_{hi,k} = {}^{Gi}\boldsymbol{R}_w^{-1}\begin{bmatrix}F_{xi,k} & 0 & 0\end{bmatrix}^{\mathrm{T}} \tag{18}$$

where $\boldsymbol{F}_{vi,k}$ is the vertical force of the spring i and $\boldsymbol{F}_{hi,k}$ is its horizontal force, both expressed in the world coordinates.

B. Unobservable State Computation

All but one springs are observed by cameras and the state of the remaining one can be computed by means of the resultant force. The force sensor provides the current resultant force, $\boldsymbol{F}_k$, that all holes exert on all objects, and the decomposition into the vertical axis and the horizontal plane results in

$$\boldsymbol{F}_{v,k} = (\boldsymbol{F}_k\cdot\boldsymbol{z}_w)\,\boldsymbol{z}_w, \quad \boldsymbol{F}_{h,k} = \boldsymbol{z}_w\times\boldsymbol{F}_k\times\boldsymbol{z}_w \tag{19}$$

where $\boldsymbol{F}_{v,k}$ and $\boldsymbol{F}_{h,k}$ are the resultant vertical and horizontal forces. Label the remaining spring as n and the force on it can be computed

$$\boldsymbol{F}_{hn,k} = \boldsymbol{F}_{h,k} - \sum_{i=1}^{n-1}\boldsymbol{F}_{hi,k}, \quad \boldsymbol{F}_{vn,k} = \boldsymbol{F}_{v,k} - \sum_{i=1}^{n-1}\boldsymbol{F}_{vi,k} \tag{20}$$

where $\boldsymbol{F}_{vn,k}$ and $\boldsymbol{F}_{hn,k}$ are the vertical and horizontal forces of the spring n.

Since θ_n is quite small, the spring's offset and force are one-to-one correspondence. Therefore, with known spring force, we can use a searching method to calculate the corresponding spring state. Resorting to (4) and (5), the following condition holds:

$$x_{en,k} = \frac{\|\boldsymbol{F}_{hn,k}\|_2}{\|\boldsymbol{F}_{vn,k}\|_2}z_{en,k}. \tag{21}$$

It restricts the relationship between the vertical and horizontal offsets of the spring's ends. In application, due to disturbances, we use an inequality to express this restriction. Therefore, the optimization problem can be expressed as

$$\begin{aligned}\min_{x_{en,k},z_{en,k}} &\left\|\frac{L_0Kz_{en,k}}{\|\boldsymbol{F}_{vn,k}\|_2+Kz_{en,k}} - \int_0^{z_{zn,k}}\sqrt{1+(3a_nz_n^2+2b_nz_n)^2}dz_n\right\| \\ \text{s.t. } &\|x_{en,k}\|\boldsymbol{F}_{vn,k}\|_2 - \|\boldsymbol{F}_{hn,k}\|_2z_{en,k}\| < \varepsilon_1 \\ &\left\|z_{en,k} - \sum_{j=1}^{n-1}\frac{z_{ej,k}}{n-1}\right\| < \varepsilon_2\end{aligned} \tag{22}$$

where ε_1 and ε_2 are two positive parameters. In the optimization objective, the first part of the function to be minimized is the spring length computed from (4) and the other part is the spring length obtained from (3). In the constraint functions, the first inequality expresses the restriction of (21) and the last one limits the value range of z_{en}. To optimize the above function, we use the previous value as the initial assignment and SNOPT as the optimization tool. The spring state $(x_{en,k}, z_{en,k})$ is obtained by optimizing the above function.

V. Insertion Strategy

For the parallel insertion of multiple objects, each connected with a spring, we propose the following insertion controller:

$$\begin{cases}\Delta\boldsymbol{v}_{k+1} = \xi_k\Delta\boldsymbol{v}_k \\ \Delta\boldsymbol{h}_{k+1} = \frac{1}{K_{h,k}}\left[K_p\left(\boldsymbol{F}_{h,k}-\boldsymbol{F}_{h,k-1}\right)+K_i\boldsymbol{F}_{h,k}\right]\end{cases} \tag{23}$$

where $\Delta\boldsymbol{v}_k$ is the current vertical insertion vector, $\Delta\boldsymbol{h}_k$ is the current horizontal compensation vector, ξ_k is a parameter between two consecutive insertions, K_p and K_i are the proportional and integral parameters, and $K_{h,k}$ is the current horizontal compliance. In this controller, the horizontal compensation is based on resultant forces and an incremental proportional integral (PI) controller is used to move the manipulator to the position where the horizontal force generated from holes is counteracted. This PI controller output dividing the insertion stiffness turns to be the desired compensational movement. The vertical insertion mainly relies on the parameter ξ_k and it is planned to efficiently fulfill insertions considering the previous performance, the contact force, and the spring state, which is introduced as follows.

As the manipulator inserts, the springs are compressed and the objects' vertical movements may not equal the insertion depth increment. A parameter is defined to represent this difference

$$\sigma_{i,k} = 1 + \frac{z_{ei,k}-z_{ei,k-1}}{\|\Delta\boldsymbol{v}_k\|_2} \tag{24}$$

where $\sigma_{i,k}$ is the insertion ratio of the group i between its object and the manipulator. This ratio reflects the insertion transmission: $\sigma_{i,k}<1$ means the object inserts less and the spring is more compressed; $\sigma_{i,k}=1$ means the spring's vertical offset unchanged; and otherwise a part of spring energy is released and the object inserts more. Estimation of the next insertion ratio by means of multiple past ratios yields

$$\overline{\sigma}_{i,k+1} = \gamma_1\sigma_{i,k} + (1-\gamma_1)\frac{\sum_{j=0}^{m_1-1}\gamma_2^j\sigma_{i,k-j}}{\sum_{j=0}^{m_1-1}\gamma_2^j} \tag{25}$$

where $\overline{\sigma}_{i,k+1}$ stands for the estimated next ratio, γ_1 and γ_2 are discounted parameters, and m_1 means how many previous ratios are used. To estimate the next ratio, this equation discounts the sum of the current ratio and the discounted multiple previous ratios. The estimated ratio can be easily verified after insertion and we use a confidence parameter to represent how much the estimated ratio can be trusted

$$\mathscr{C}_{i,k+1} = \frac{\sum_{j=0}^{m_2-1}\gamma_3^j e^{\left(T_1-\frac{\|\sigma_{i,k-j+1}-\overline{\sigma}_{i,k-j+1}\|}{\sigma_{i,k-j+1}}\right)}}{\sum_{j=0}^{m_2-1}\gamma_3^j}\mathscr{C}_{i,k} \tag{26}$$

where $\mathscr{C}_{i,k}\in[0,1]$ is the confidence parameter iterated in each step, depending on the difference of the estimated insertion ratio and the real one, m_2 is the averaging number, γ_3 is a discounted

parameter, and $T_1 \in (0,1)$ is the parameter above which the confidence on ratio estimation grows. The above equation uses an exponential function to aggressively increase the confidence parameter and conservatively reduce it. In parallel insertion, there are multiple sizes of the springs' compression and we pick the most compressed one, labelled with a subscript c, to compute the expected overall insertion ratio. The most compressed spring means its connecting object has the least insertion depth and we use it to plan for the whole insertion. This yields

$$\tilde{\sigma}_{k+1} = \mathscr{C}_{c,k}\overline{\sigma}_{c,k+1} + (1-\mathscr{C}_{c,k})\sum_{i=1}^{n}\frac{\overline{\sigma}_{i,k+1}}{n} \tag{27}$$

where $\tilde{\sigma}_{k+1}$ is the expected insertion ratio for the next manipulator insertion. This equation determines the expected overall insertion ratio using the sum of the estimated ratio of the most compressed spring multiplying its corresponding confidence parameter and the unconfident proportion multiplying the average estimated ratio of all groups.

A large horizontal force shows an incorrect alignment viewing the n groups as a whole and the insertion needs to slow down giving priority to compensation. An exponential relationship is presented between the horizontal force and its effect parameter to insertion

$$\lambda_k = 2e^{-\frac{\ln 2\|\boldsymbol{F}_{h,k}\|_2}{T_2}} \tag{28}$$

where $\lambda_k \in (0,2]$ is the effect parameter of the horizontal force to insertion and T_2 is a positive parameter. It means that λ_k equals one if the resultant horizontal force equals T_2 and the horizontal force has no effect on the insertion; a smaller λ_k means the gripper needs large horizontal compensation and the insertion slows; and $\lambda_k > 1$ indicates the horizontal force is well constrained and the insertion can enlarge its depth increment.

Even when the resultant horizontal force is zero, the springs' horizontal offsets may still exist and this affects the single insertion. Therefore, we consider the springs' horizontal offsets in insertion planning and define the following parameter:

$$\chi_k = e^{-\frac{\gamma_4\sum_{i=1}^{n}\|x_{ei,k}\|}{n}} \tag{29}$$

where $\chi_k \in (0,1]$ is the effect parameter of the horizontal offsets to insertion and γ_4 is a scaling parameter. A large average horizontal offset slows the insertion.

Combining the above results leads to the expected insertion

$$\Delta\overline{v}_{k+1} = \frac{\lambda_k\chi_k\left(\|\Delta\boldsymbol{v}_k\|_2 + z_{ec,k} - z_{ec,k-1}\right)}{\tilde{\sigma}_{k+1}} \tag{30}$$

where $\Delta\overline{v}_{k+1}$ is the expected insertion of the next step. In this equation, the bracket includes the insertion of the most compressed object; it multiplies the parameters λ_k and χ_k, resulting in the effect of the horizontal state of the group c to insertion; and then it is divided by the expected insertion ratio to obtain the manipulator's expected insertion. Limiting this result and dividing it by the current insertion depth increment leads to the insertion parameter

$$\xi_k = \frac{\min\left\{\Delta\overline{v}_{k+1}, \Delta v_{\max}\right\}}{\|\Delta\boldsymbol{v}_k\|_2} \tag{31}$$

where $\Delta v_{\max}$ is the maximum allowed insertion depth increment.

Although the manipulator's insertion is the same for all groups, due to unexpected disturbances, the springs' compression is different and the objects do not reach their terminal states, usually the bottom of the holes, simultaneously. Therefore, the terminal condition is set as

$$\|\mathscr{L}_{c,k} - \mathscr{L}\| < \varepsilon_L,\ \max_{i=1,\ldots,n}\sigma_{i,k} < \varepsilon_\sigma,\ \|\boldsymbol{F}_{v,k}\|_2 - F_{v,m} > 0 \tag{32}$$

where $\mathscr{L}_{c,k} = \sum_{j=0}^{k}\|\Delta\boldsymbol{v}_j\|_2 + z_{ec,k} - L_0$ is the insertion length of the most compressed object, $\mathscr{L}$ is the object's desired insertion length, ε_L and ε_σ are positive parameters, and $F_{v,m}$ is the vertical force threshold. The above inequalities verify the terminal state is reached from three aspects: the insertion length, the insertion ratio, and the vertical force. The insertion length condition only focuses on the group with the most compressed spring, to ensure that all objects touch down the bottom. In the insertion ratio condition the maximum ratio is chosen and compared with the threshold, making sure no object inserts. The force condition considers the vertical force of all the springs.

Fig. 4 shows the control process for parallel insertion. With observations of $2(n-1)$ microscopes, the $n-1$ springs' states are acquired using the fitting and optimization method and furthermore the forces on their ends are computed resorting to (4) and (5). The force sensor provides the resultant force exerted on all objects and subtracting the other $n-1$ springs' forces leads to the force upon the remaining object, whose state is computed via optimization. After acquiring all springs' states, the horizontal stiffness is obtained and with the resultant force the horizontal compensation is determined. Meanwhile, the insertion ratio of every spring is calculated, together with its estimation of the next step; confidence parameters of every group are then computed according to the error between the estimated and the true ratios; and the expected insertion ratio for the overall insertion is obtained using the insertion ratio, the confidence parameter of the most compressed spring, and the average estimated insertion ratio. The offset and force effect parameters are the results of evaluating the current insertion depth increment and the compensation effect. The expected insertion is then determined and limited by its maximum permission. Three aspects are evaluated to check if the terminal condition is reached, including the insertion length, the insertion ratio, and the vertical force. If not, the horizontal compensation and the vertical insertion activate.

VI. Experiments

On the precision assembly platform shown in Fig. 5, we test the proposed approaches including the spring model, the visual-based state acquisition, and the insertion strategy. The experimental platform equips with three microscopes, two force sensors, and six robot arms. This experiment only employs two robot arms, two microscopes, and a force sensor to fulfill the parallel insertion. The upper arm, which holds the parallel gripper, is equipped with three Suguar KWG06030-G, with translational resolution as $\pm 0.5\ \mu$m, and a two-DOF manual tilt

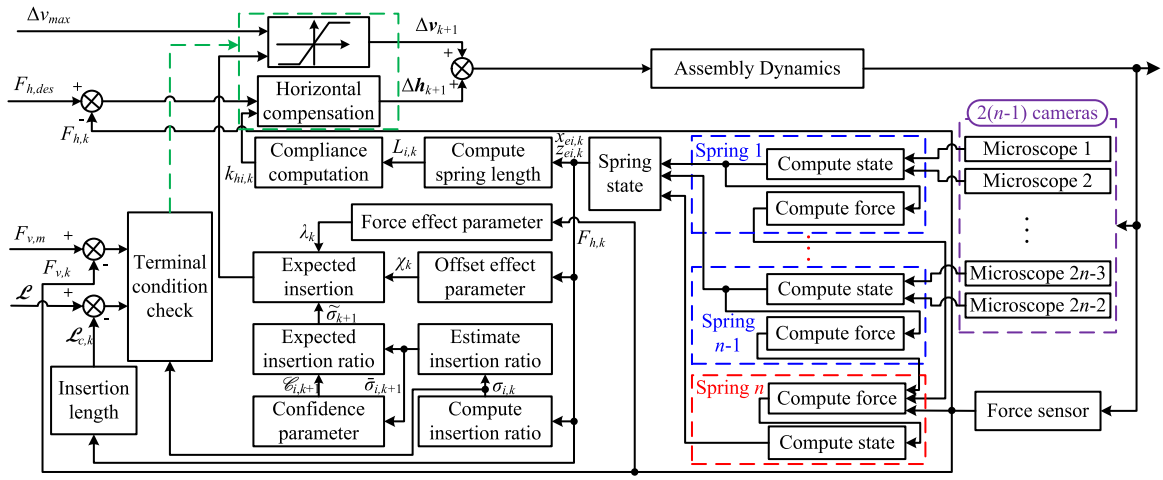

Fig. 4. Process for parallel insertion control.

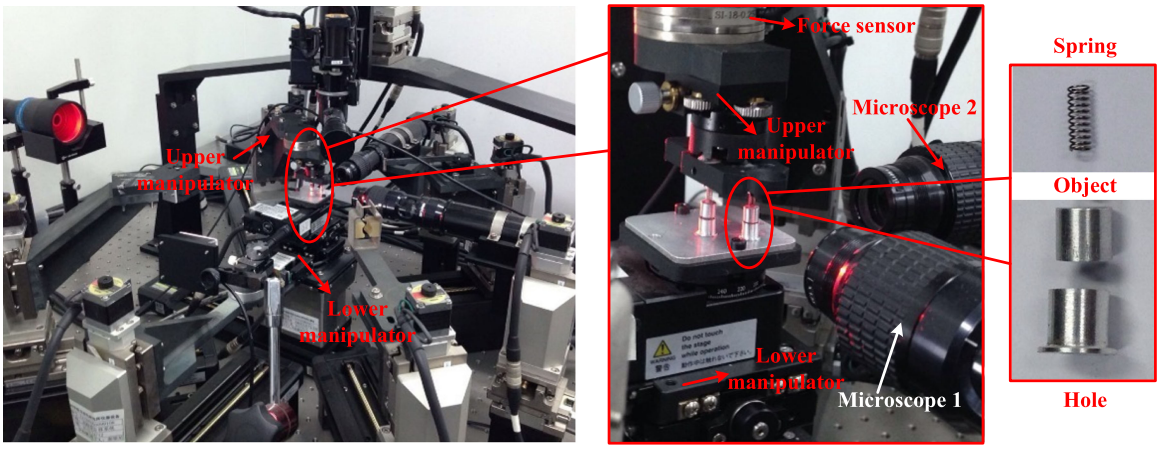

Fig. 5. Experiment platform and the objects to be assembled.

adjustment Sigma KKD-25C. The lower arm, which grips the holes, has a Micos ES-100 with movement errors within 0.1 μm, and KGW06050-L, KGW06075-L, and SGSP-40yaw for rotation. One microscope is GC2450 with resolution of 2448 $\times$ 2050 pixels and another is PointGrey 50S5M-C whose resolution is 2448 $\times$ 2048 pixels. The microscopes locate on platforms, each driven by three Suguar KWG06030-G to follow the insertion, which facilitate auto adjusting the springs to the center of the image and clearly viewing the springs. The force sensor is Nano-43 with resolution of 1/128 N, which can be improved with filtering. Restricted by the platform configuration, we only test the parallel insertion of two groups. The two objects are hollow and cylinder shaped, with 0.1 mm thickness, 5 mm length, and 5 mm diameter. The two holes are hollow cylinders with 50 μm thickness and 5 mm length. The materials are aluminum and their interferences range in $0\sim5$ μm. Two compression springs are 5 mm long and their diameters are both 2.5 mm. Since this paper mainly focuses on the insertion strategy of this parallel passive configuration, the springs are glued to the objects and dissolved with solvent after assembly, for easy realization, and in future we will design appropriate mechanisms to connect springs and objects.

To acquire the spring coefficient, we compress the spring, record the compression lengths and the corresponding forces, repeat these processes for several times, and average the ratios between forces and compressed lengths, which leads to $K = 27.4\,\mathrm{mN}/\mu\mathrm{m}$. The Butterworth method is used to filter the force sensor.

We first verify the spring model by comparing the computed forces and the measured ones. To do that, one object is inserted into a hole so that its posture is unchanged and the spring is compressed. Given a randomized initial setting, we sequently move the upper manipulator 20 steps of 10 μm along the positive x-axis, the positive y-axis, the negative x-axis, and then the negative y-axis, in its own coordinates. Between two steps, the force change is chosen as the comparison objective. According to the relative displacements of every manipulator and the corresponding measured forces, the spring's initial offset is obtained by optimizing the squared errors between the forces computed with the spring model and measured from the sensor. The forces computed with the proposed spring model are then acquired according to the motion steps and the relative forces are calculated between two consecutive movements. Fig. 6 shows the comparison results where the first two subfigures present

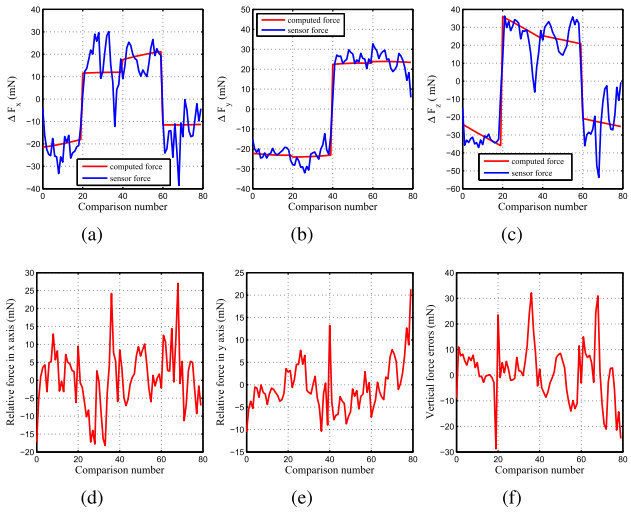

Fig. 6. Comparison between the forces computed from the spring model and measured from the force sensor. The first row is the relative forces in the x, y, and z axes between two consecutive states; and the rest is the horizontal and vertical errors between the computed force and the measured force.

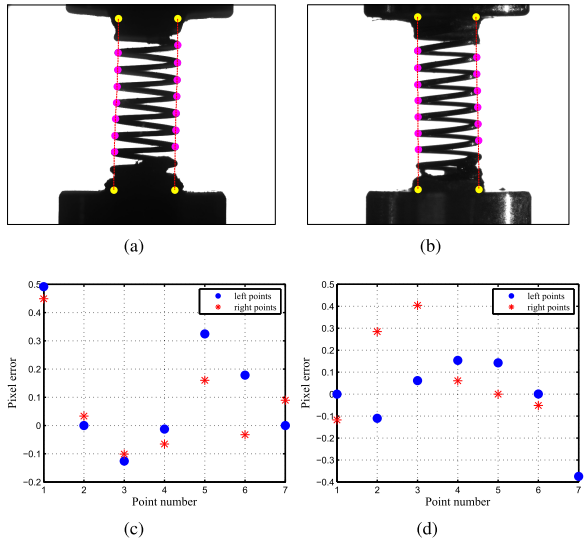

Fig. 7. Fitting curve of the spring's edge points and the errors between the computed and the true values. (a) Fitting curve of the spring viewed in the microscope 1. (b) Fitting curve of the spring viewed in the microscope 2. (c) Errors between the computed and the true values in the first image. (d) Errors between the computed and the true values in the second image.

the relative forces in the horizontal plane and the errors between them are shown in the fourth and fifth subfigures. It can be seen that the computed forces fit the measured forces and most of their errors range in $\pm 20\,\text{mN}$. The statistical errors may originate from the object manufacturing precision and the contact that are not explicitly modeled. The mean errors are $\mu_x = -2.03\,\text{mN}$ and $\mu_y = -0.60\,\text{mN}$, and the standard deviations are $\sigma_x = 11.34\,\text{mN}$ and $\sigma_y = 4.83\,\text{mN}$. Fig. 6(c) shows the relative vertical forces and Fig. 6(f) displays their errors. The mean error is $\mu_z = 1.06\,\text{mN}$ and the standard deviation is $\sigma_z = 11.08\,\text{mN}$. Known from these results, the spring model can relate the spring force and offset with a tolerant error.

The second experiment aims at verifying the method of vision based offset acquisition. As shown in Fig. 7, the two ends of the spring are blocked. We randomly pick a state where the spring is compressed and the spring's two ends deviate. Using the two horizontal microscopes, the spring images are obtained and the key points on the coils are located using Canny operator and circular Hough Transform, which are circled as magenta points. In the proposed method, we set the manipulator's bottom surface and the object's upper surface as the initialization for optimization and a piecewise function is obtained to fit the detected points. The fitted top and bottom ends are marked as the yellow points and the dotted lines are the fitting curves. Fig. 7(c) and (d) present the horizontal pixel errors between the circled points and their fitted values. Known from these figures, the fitting errors are limited in a small ranges: for Fig. 7(a), the mean errors are $\mu_{1l} = -0.02$ pixels and $\mu_{1r} = -0.02$ pixels, and the standard deviations are $\sigma_{1l} = 0.04$ pixels and $\sigma_{1r} = 0.13$ pixels; and for Fig. 7(b), the mean errors are $\mu_{2l} = -0.03$ pixels and $\mu_{2r} = -0.16$ pixels, and the standard deviations are $\sigma_{2l} = 0.02$ pixels and $\sigma_{2r} = 0.04$ pixels. We also test multiple images and the overall fitting error maintains small, which shows the correctness of the spring's offset acquisition method. The errors from the visual detection, as shown in Fig. 7, are limited in a small range and lead to a not-large contact force after multiplying the spring horizontal stiffness, which is obtained in the next experiment. These errors may affect the insertion planning process resorting to (29), rather than the horizontal compensation [recalling (23)].

TABLE I
CONTROL PARAMETERS FOR EXPERIMENTS

T_1	$F_{v,m}$	ε_σ	γ_1	γ_2	m_1	K_p
0.2	0.5N	0.1	0.5	0.9	5	0.3
T_2	Δv_{max}	ε_L	γ_3	γ_4	m_2	K_i
$100\mu m$	$20\mu m$	$1\mu m$	0.1	0.9	5	0.5

The third experiment is carried out to test the parallel insertion strategy. The control parameters are given in Table I, where the objects are expected to be inserted with a maximum increment 20 μm and the process ends after the vertical force surpasses 0.5 N. We use the Ziegler–Nichols method to regulate the controller parameters. To counteract the errors of initialization settings, the relative state change is used rather than the absolute value, i.e., the errors relative to the initial offset are labeled as the spring's states. Fig. 8 shows the experiment results. The insertion can be classified into two parts: in the first 170 steps, the force magnitude and variation are relative small while in the latter half, due to disturbances, they become large. After the insertion starts, the springs are compressed to balance the friction forces caused by the interferences and the vertical force stabilizes at about 100 mN. In the first half, the variation of the contact forces ranges in $[-20, 20]$ mN in the x-axis, $[-10, 10]$ mN in the y-axis, and $[-120, -80]$ mN in the z-axis.

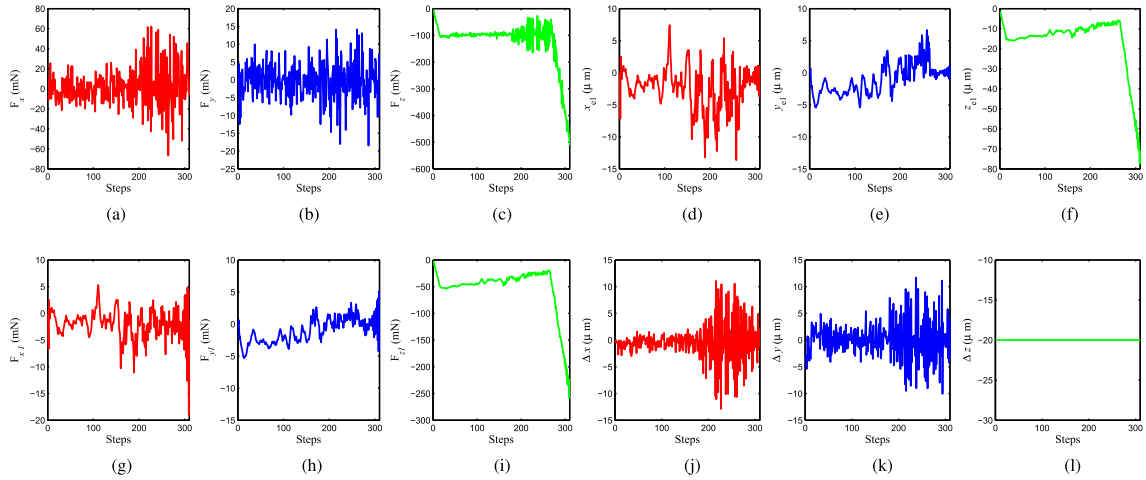

Fig. 8. Experiment results for the parallel insertion of two groups of objects. (a)–(c) Forces in the x, y, and z axes measured from the force sensor. (d)–(f) the spring offsets in the x, y, and z axes of the object viewed in the microscopes. (g)–(i) the forces in the x, y, and z axes computed using the vision-based method. (j)–(l) the insertion movements in the x, y, and z axes.

These resultant forces show that they maintain in a small range as inserting and as a whole the objects are well aligned. The spring offsets viewed in microscopes also vary: $[-10, 5]$ μm in the x-axis, $[-5, 0]$ μm in the y-axis, and $[-17, -10]$ μm in the z-axis. According to these values, the corresponding forces on this object are computed based on the spring model, which are shown in Fig. 8(g)–(i). Subtracting these computed forces from the resultant ones results in the forces upon the other object, and using the optimization method the other object's offsets are obtained. With both objects' offsets, the vertical insertion is planned. The last three subfigures in Fig. 8 present the manipulator movements: the horizontal compensations range in $[-10, 10]$ μm and the vertical insertion always takes the maximum increments. As the insertion enters the latter half, the vibration of the contact force becomes large, and accordingly the observed spring's offsets, the computed forces, and the manipulator movements also grow. The horizontal force can be compensated for and the vertical insertion is not affected. As the object reaches the bottom at about 270 steps, the upper manipulator still inserts and the spring is more compressed until F_{vm} is surpassed. In the state with the largest horizontal force, the horizontal stiffness of this parallel insertion is close to 4.4 mN/μm. We have also experimented to acquire the proportionality of the deformation between objects and the exerted force, which is about 60 mN/μm. Compared with the parallel rigid insertion, this parallel compliant configuration has much less horizontal stiffness.

The errors in Fig. 8 may come from the machining errors and disturbances which become severer as the spring number grows. The result variations are originated from the compensation and disturbances. A deviation exists between the insertion direction and the vertical axis in the view plane of microscopes. This deviation constantly generates horizontal alignment errors in each insertion step and the controller intends to compensate for the horizontal forces.

As the spring number grows, the horizontal stiffness basically increases, as shown in (10), and the resultant horizontal force grows as well. These two increments will affect the horizontal compensation performance, e.g., bigger variations. Another effect comes from the vertical insertion planning and the insertion probably becomes slower due to the increment of the horizontal force, according to (28). The averaging in the equation and the tuning of the parameter γ_4 help to reduce the effect of the visual detection errors.

The results would not be different if the test is executed in industry environment. But due to the property of microscopes and the precision requirement, the mechanism needs to locate on an isolation platform in a clean room.

VII. Conclusion

This paper considers the parallel insertion of multiple objects connected with passive compliant mechanisms in precision assembly. This configuration can provide substantial compliance to parallel insertion and improve efficiency for massive precision assembly. We analyze the compliance of parallel springs and build a model to relate the spring's state and force. In rigid parallel insertion, the state of each object is unobservable since it is blocked, while in this configuration we use two microscopes to observe one spring and obtain its state employing a fitting and optimization approach, which is applied to all but one springs. The state of the remaining spring is acquired via the resultant force provided by a force sensor. A strategy is proposed to efficiently insert multiple objects simultaneously while considering the resultant force, all springs' offsets, and the insertion ratio. Experiments are implemented to validate the proposed method.

Appendix A
Parameter Acquisition of the Spring Function

Reviewing the description in the first two paragraphs in Section III-A, we use two points to compute the parameters in (1). At the top end of the spring, P_{0i}, its slope is zero and its position is the origin, which leads to

$$P_{0i} : \begin{cases} c_i = 0 \\ d_i = 0. \end{cases} \tag{33}$$

At the bottom end of the spring, P_{ei}, its position can be extracted and its slope is determined by θ_i

$$P_{ei}: \begin{cases} a_i x_{ei}^3 + b_i x_{ei}^2 + c_i x_{ei} + d_i = z_{ei} \\ 3a_i x_{ei}^2 + 2b_i x_{ei} + c_i = \tan\theta_i. \end{cases} \tag{34}$$

Solving the above equations lead to the results in (2).

REFERENCES

[1] H. V. Brussel *et al.*, "Assembly of microsystems," *CIRP Ann-Manuf. Technol.*, vol. 49, no. 2, pp. 451–472, 2000.

[2] B. Tamadazte, N. L. Piat, and S. Dembele, "Robotic micromanipulation and microassembly using monoview and multiscale visual servoing," *IEEE/ASME Trans. Mechatronics*, vol. 16, no. 2, pp. 277–287, Apr. 2011.

[3] F. Shen, W. Wu, D. Yu, D. Xu, and Z. Cao, "High-Precision automated 3-D assembly with attitude adjustment performed by LMTI and vision-based control," *IEEE/ASME Trans. Mechatronics*, vol. 20, no. 4, pp. 1777–1789, Aug. 2015.

[4] D. Xing, F. Liu, S. Liu, and D. Xu, "Motion control for cylindrical objects in microscopes view using a projection method: I. collision detection and detach control," *IEEE Trans. Ind. Electron.*, vol. 64, no. 7, pp. 5524–5533, Jul. 2017.

[5] J. D. Wason, J. T. Wen, J. J. Gorman, and N. G. Dagalakis, "Automated multiprobe microassembly using vision feedback," *IEEE Trans. Robot.*, vol. 28, no. 5, pp. 1090–1103, Oct. 2012.

[6] D. Xing, F. Liu, F. Qin, and D. Xu, "Coordinated insertion control for inclined precision assembly," *IEEE Trans. Ind. Electron.*, vol. 63, no. 5, pp. 2990–2999, May 2016.

[7] S. Liu, Y. Li, D. Xing, D. Xu, and H. Su, "An efficient insertion control method for precision assembly of cylindrical components," *IEEE Trans. Ind. Electron.*, vol. 64, no. 12, pp. 9355–9365, Dec. 2017.

[8] Z. Xu, Z. Liu, H. Liu, Z. Yin, Y. Huang, and J. Chen, "Analytical evaluation of interfacial crack propagation in vacuum-based picking-up process," *IEEE Trans. Compon. Packag. Manuf. Technol.*, vol. 5, no. 11, pp. 1700–1708, Nov. 2015.

[9] F. Qin, D. Zhang, D. Xing, D. Xu, and J. Li, "Laser beam pointing control with piezoelectric actuator model learning," *IEEE Trans. Syst., Man, Cybern., Syst.*, to be published.

[10] H. Hu, M. Zhou, Z. Li, and Y. Tang, "Deadlock-Free control of automated manufacturing systems with flexible routes and assembly operations using petri nets," *IEEE Trans. Ind. Inform.*, vol. 9, no. 1, pp. 109–121, Feb. 2013.

[11] Y. Bang, K. Lee, J. Kook, W. Lee, and I. Kim, "Micro parts assembly system with micro gripper and RCC unit," *IEEE Trans. Robot.*, vol. 21, no. 3, pp. 465–470, Jun. 2005.

[12] Q. Xu, "Design and smooth position/force switching control of a miniature gripper for automated microhandling," *IEEE Trans. Ind. Inform.*, vol. 10, no. 2, pp. 1023–11032, May 2014.

[13] R. K. Jain, S. Majumder, and A. Dutta, "SCARA based peg-in-hole assembly using compliant IPMC micro gripper," *Robot. Auton. Syst.*, vol. 61, no. 3, pp. 297–311, 2013.

[14] D. Xing, D. Xu, F. Liu, H. Li, and Z. Zhang, "Precision assembly among multiple thin objects with various fit types," *IEEE/ASME Trans. Mechatronics*, vol. 21, no. 1, pp. 364–378, Feb. 2016.

[15] S. Jin *et al.*, "Point-Based solution using Jacobian-Torsor theory into partial parallel chains for revolving components assembly," *J. Manuf. Syst.*, vol. 46, pp. 46–58, 2018.

[16] H. Maruyama, R. Iitsuka, K. Onda, and F. Arai, "Massive parallel assembly of microbeads for fabrication of microtools having spherical structure and powerful laser manipulation," in *Proc. IEEE Int. Conf. Robot. Autom.*, 2010, pp. 482–487.

[17] H. K. Chu, J. K. Mills, and W. L. Cleghorn, "Fabrication of a microcoil through parallel microassembly," in *Proc. IEEE Int. Conf. Robot. Autom.*, 2012, pp. 5050–5055.

[18] B. Chang, A. Virta, and Q. Zhou, "Hybrid microassembly for massively parallel assembly of microchips with water mist," in *Proc. IEEE Int. Conf. Manipulation Manuf. Meas. Nanosci.*, 2012, pp. 38–43.

[19] G. Skidmore *et al.*, "Parallel assembly of microsystems using Si micro electro mechanical systems," *Microelectron. Eng.*, vol. 67–68, pp. 445–452, 2003.

Dengpeng Xing received the B.S. degree in mechanical electronics and the M.S. degree in mechanical manufacturing and automation from Tianjin University, Tianjin, China, in 2002 and 2006, respectively, and the Ph.D. degree in control science and engineering from Shanghai Jiao Tong University, Shanghai, China, in 2010.

He is currently an Associate Professor with the Research Center of Precision Sensing and Control, Institute of Automation, Chinese Academy of Sciences, Beijing, China. His research interests include robot control and learning, precision assembly, and optimization.

Yan Lv received the B.S. and Ph.D. degrees in mechanical manufacturing and automation from Zhejiang University, Hangzhou, China, in 2005 and 2012, respectively.

She is currently a Lecturer with the School of Engineering, Zhejiang A&F University, Hangzhou, China. Her research interests include intelligent manufacturing, mathematic modeling of knowledge in manufacturing process.

Song Liu received the B.S. degree in sensing technology and instrumentation from Shandong University, Jinan, China, in 2012, and the Ph.D. degrees in control science and engineering from the University of Chinese Academy of Sciences, Beijing, China, and the City University of Hong Kong (CityU), Hong Kong, China, respectively, in 2017.

From June 2017 to 2018, he served as a Postdoctoral Fellow with the Robot Vision Research Lab, Department of Mechanical Engineering, CityU. He is currently working as a Postdoctoral Fellow with MEMS Group, University of Southern California, Los Angeles, CA, USA. His current research interests include ultrasonic MEMS, SFAT, visual servo control, and robot learning.

De Xu (M'05–SM'09) received the B.S. and M.S. degrees in control science and engineering from the Shandong University of Technology, Jinan, China, in 1985 and 1990, respectively, and the Ph.D. degree in control science and engineering from Zhejiang University, Hangzhou, China, in 2001.

Since 2001, he has been with the Institute of Automation, Chinese Academy of Sciences, Beijing, China, where he is currently a Professor with the Research Center of Precision Sensing and Control. His research interests involve robotics and automation, in particular, the control of robots, such as visual control and intelligent control.

Fangfang Liu received the B.S. and Ph.D. degrees in mechanical electronics from Zhejiang University, Hangzhou, China, in 2006 and 2012, respectively.

She is currently an Associate Professor with the Research Center of Precision Sensing and Control, Institute of Automation, Chinese Academy of Sciences, Beijing, China. Her research interests include precision mechanical design and mechatronic control.